Comput Mech
DOI 10.1007/s00466-017-1412-5

ORIGINAL PAPER

Fully coupled simulation of multiple hydraulic fractures to propagate simultaneously from a perforated horizontal wellbore

Qinglei Zeng[1] · Zhanli Liu[1] · Tao Wang[1] · Yue Gao[1] · Zhuo Zhuang[1]

Received: 13 December 2016 / Accepted: 10 April 2017

Abstract In hydraulic fracturing process in shale rock, multiple fractures perpendicular to a horizontal wellbore are usually driven to propagate simultaneously by the pumping operation. In this paper, a numerical method is developed for the propagation of multiple hydraulic fractures (HFs) by fully coupling the deformation and fracturing of solid formation, fluid flow in fractures, fluid partitioning through a horizontal wellbore and perforation entry loss effect. The extended finite element method (XFEM) is adopted to model arbitrary growth of the fractures. Newton's iteration is proposed to solve these fully coupled nonlinear equations, which is more efficient comparing to the widely adopted fixed-point iteration in the literatures and avoids the need to impose fluid pressure boundary condition when solving flow equations. A secant iterative method based on the stress intensity factor (SIF) is proposed to capture different propagation velocities of multiple fractures. The numerical results are compared with theoretical solutions in literatures to verify the accuracy of the method. The simultaneous propagation of multiple HFs is simulated by the newly proposed algorithm. The coupled influences of propagation regime, stress interaction, wellbore pressure loss and perforation entry loss on simultaneous propagation of multiple HFs are investigated.

Keywords Multiple hydraulic fractures · Fluid partitioning · XFEM · Fully coupled simulation · Perforation entry loss

✉ Zhanli Liu
liuzhanli@tsinghua.edu.cn

✉ Zhuo Zhuang
zhuangz@tsinghua.edu.cn

1 Applied Mechanics Laboratory, School of Aerospace Engineering, Tsinghua University, Beijing 100084, China

1 Introduction

The propagation of multiple fractures driven by the flow of viscous fluid, also known as hydraulic fractures, can occur both naturally and in engineering applications. For example, several dikes may ascend from a deep pressurized magma chamber simultaneously [1] or multiple cracks, in much smaller scales, can initiate at cell-cell junctions in epithelial tissues and driven to propagate by the fluid in the extracellular matrix [2]. In recent years, hydraulic fracturing has attracted great attention in petroleum industry, which serves as an appealing technique in promoting the productivity of unconventional shale gas and oil. In order to increase operating efficiency and reduce the cost in engineering field, multi-stage hydraulic fracturing from a horizontal wellbore is widely employed to stimulate the reservoirs. In each fracturing stage, several clusters of perforations are placed along the horizontal wellbore. The fractures are initiated from the clusters and then driven to propagate simultaneously by the pumping operation through the wellbore. Multiple HFs are desired to propagate with almost the same lengths to stimulate the formations as much as possible.

A lot of efforts have been dedicated to the research of hydraulic fracturing both analytically and numerically in the literature, especially for the propagation of a single HF. The analytical research can trace back to the classical and widely used KGD model [3,4] (named after pioneering researchers Kristianovic, Geertsma, and de Klerk) and PKN model [5,6] (named after Perkins, Kern and Nordgren). For a HF with plane strain assumption or a single radial HF, some analytical and asymptotic solutions are also available in the literature [7–11]. As for the propagation of multiple HFs, few analytical solutions exist. Compared with the propagation of one single HF, the problem including multiple HFs is cumbersome because of the stress interaction between dif-

Published online: 04 May 2017

ferent fractures and the interconnected fluid flow system. As for the effect of stress interaction, stability analysis has been carried out for the propagation of multiple cracks in elastic brittle solid medium [12–15]. Uniform growth of all cracks can be obtained in stable system, while in unstable system some cracks may stop growing and the others grow faster, which is called preferential growth. In these stability analyses the fluid flow is not included. However, in hydraulic fracturing, the fluid flow is the dominated driving force and can't be ignored in the analysis process. Olson et al. [16] and Taleghani [17] studied the propagation of multiple HFs but each fracture was treated independently. The fluid flows in different fractures are interconnected by a fluid source region. In hydraulic fracturing treatments, the fluid source region is in the horizontal wellbore and in magma intrusion it's in the pressurized chamber. The partitioning of the fluid into different fractures from the source region is crucial for the propagation of multiple HFs. Mack et al. [18] simulated multilayer fracture treatments numerically assuming that the fractures are separated by well-defined stress barriers which excludes the stress interaction effect and the behavior of each fracture is governed by PKN model or pseudo-three-dimensional model.

In order to better understand the mechanism of the propagation of multiple HFs and optimize engineering designs, it is important to model the fully coupled problem considering the stress interaction and solving the fluid flow system. Bunger et al. [19] derived the theoretical approximation of the energy required to propagate multiple parallel HFs and concluded that an energetically optimal spacing exists for multiple HFs. However, the theoretical approximation is limited to the cases with more than five HFs, but in practice three to eight HFs are typically propagating simultaneously. Lecampion and Desroches [20], Wu and Olson [21] considered the fluid flow in the horizontal wellbore and solved the elasticity equations with displacement discontinuity method.

In this paper, a fully coupled numerical method is developed to simulate the propagation of multiple HFs by XFEM, which can model arbitrary fracture propagation without remeshing. As an enhanced finite element method, XFEM can also handle problems with a variety of materials including plasticity, damage or inhomogeneity and complex reservoir structures, like multilayer reservoirs and extensive natural fractures. It's also convenient to consider other physical fields, like seepage or temperature fields. It has been successfully employed to model the propagation of one single HF or multiple non-interconnected HFs [17,22–27]. The deformation of solid formation, fluid flow in the fractures and fluid flow in the horizontal wellbore are fully coupled and nonlinear. In former works, the solid deformation and fluid flow system are solved separately and coupled by fixed point iteration or the Picard iteration [20,21,28]. The fixed point iteration is a first-order algorithm and converges slowly [28,29]. And more importantly, if the fluid equation is solved separately, fluid pressure at one point should be specified as the essential boundary condition, which is generally unknown a priori. One alternative way is to include the so-called solvability condition [30], which describes the global mass conservation equation. Khoei et al. [24] proposed another iteration loop to obtain the injection pressure. In this paper, we propose a Newton's iteration scheme to solve the fully coupled system and derive an integrated tangential matrix for coupled equations, which can obtain a quadratic convergence rate and avoids the need to include mass conservation equation explicitly or impose pressure boundary condition. In every time step, the growth lengths of the fractures are unknown and may be different from each other. Gordeliy and Peirce [23] adopted an implicit level set algorithm (ILSA) proposed in [31] to locate the new front for the propagation of one HF. ILSA is based on the asymptotic solutions for different propagating regimes [10] in the vicinity of fracture tips. However, for the cases with multiple HFs, the propagating regimes may vary during the propagating process because the partitioning of pumping fluid into different fractures constantly changes and it is also part of the solutions. So it is troublesome to adapt the asymptotic solutions according to the propagating regimes. In this paper, a secant iterative method based on the equivalent SIFs is proposed to update fracture fronts for a specified time increment. An interaction integral is adopted to calculate the SIFs with high accuracy.

This paper is organized as follows. In Sect. 2, the simplifications and assumptions of the model are presented and the governing equations are given for the fully coupled problem. The discretization of these equations is introduced in Sect. 3. Then Newton's iteration for the fully coupling equations and the secant iteration for fracture growth lengths are presented in Sect. 4. Several examples are given in Sect. 5 to verify the accuracy of the newly proposed method, including the propagation of viscosity-dominated and toughness-dominated fractures, as well as the initiation of two inviscid-fluid-driven fractures. In Sect. 6, the propagation of multiple HFs is modeled. The influences of propagation regimes, stress interaction, pressure loss in the wellbore and perforation entry loss on simultaneous propagation of multiple HFs are mainly investigated.

2 Theoretical model and governing equations

Consider multiple HFs propagating in an impermeable elastic medium Ω from the wellbore as shown in Fig. 1. The geometry is symmetric and only the top half is depicted. The plane strain assumption is adopted for the elastic medium. The thickness is assumed to be h. The Young's modulus and Poisson's ratio of the linear-elastic medium are denoted as E

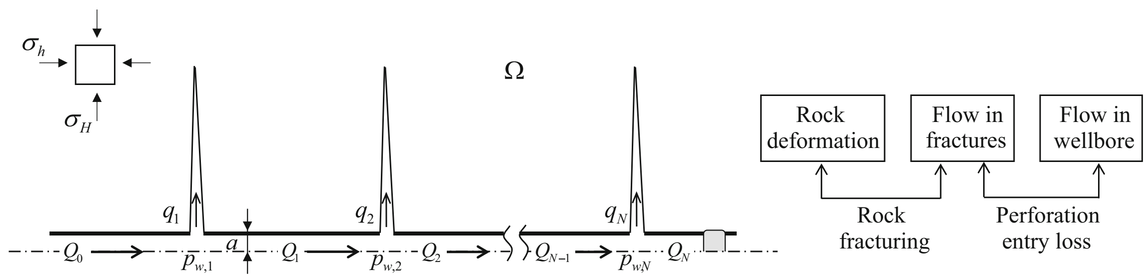

Fig. 1 Multiple HFs propagating simultaneously from a horizontal wellbore and the fully coupled problem

and ν. The casing of the wellbore is assumed to be rigid with a radius a and has no influence on the stress of solid formations. Incompressible Newtonian fluid is adopted. The number of HFs driven to propagate simultaneously is denoted as N. The inlet volume flow rate per unit thickness into half of fracture I is $q_I(I = 1, N)$ and the volume flow rate in the wellbore between fracture I and $I+1$ is $Q_I(I = 1, N-1)$. The wellbore length between fracture I and $I+1$ is $D_I(I = 1, N-1)$. The total pumping flow rate and the terminal flow rate in the wellbore are denoted as Q_0 and Q_N, respectively. The pressure $p_{w,I}(I = 1, N)$ represents the pressure value in the wellbore at the entrance of fracture I. For expression brevity the fracture length mentioned hereinafter refers to half length and is denoted as $l_I(I = 1, N)$. The principal tectonic stresses in two directions are denoted as σ_h and σ_H. Typically, σ_h is much smaller than σ_H and the fractures would propagate along the direction of σ_H.

2.1 Deformation and fracturing of the solid medium

If the body force is negligible, the stress field $\boldsymbol{\sigma}$ should satisfy the equilibrium equations

$$\nabla \cdot \boldsymbol{\sigma} = \mathbf{0} \tag{1}$$

The displacement field is denoted as $\mathbf{u}$ and the strain field $\boldsymbol{\varepsilon}$ can be calculated from the geometric equation

$$\boldsymbol{\varepsilon} = \frac{1}{2}\left[\nabla \mathbf{u} + (\nabla \mathbf{u})^{\mathrm{T}}\right] \tag{2}$$

The stress and strain should satisfy constitutive equations and for linear-elastic medium the constitutive equations can be written as

$$\boldsymbol{\sigma} = \mathbf{C} : \boldsymbol{\varepsilon} \tag{3}$$

where $\mathbf{C}$ is elastic matrix.

Assuming displacement $\bar{\mathbf{u}}$ is prescribed on the displacement boundary Γ_u, fluid pressure p acts on the fractures surfaces $\Gamma_p^+ \cup \Gamma_p^-$ and confining stress $\bar{\mathbf{t}}$ is prescribed on the external force boundary Γ_t, the boundary conditions for solid medium can be written as,

$$\mathbf{u} = \bar{\mathbf{u}} \text{ on } \Gamma_u \tag{4}$$

$$\boldsymbol{\sigma} \cdot \mathbf{n} = -p\mathbf{n} \text{ on } \Gamma_p^+ \cup \Gamma_p^- \tag{5}$$

$$\boldsymbol{\sigma} \cdot \mathbf{n} = \bar{\mathbf{t}} \text{ on } \Gamma_t \tag{6}$$

The solid problem is symmetric and only a half part model is considered.

The fracture will propagate with a deflection angle θ if the equivalent SIF K_{eq} reaches the critical value K_{Ic}, which can be computed as [32]

$$\theta = 2\arctan\frac{1}{4}\left(\frac{K_I}{K_{II}} - \mathrm{sign}(K_{II})\sqrt{\left(\frac{K_I}{K_{II}}\right)^2 + 8}\right) \tag{7}$$

where K_I and K_{II} are the SIFs corresponding to mode I and mode II. K_{eq} can be written as [32]

$$K_{eq} = \cos\frac{\theta}{2}\left(K_I\cos^2\frac{\theta}{2} - \frac{3K_{II}}{2}\sin\theta\right) \tag{8}$$

2.2 Fluid flow in the fracture

For each fracture, the fluid flow is treated as one-dimensional flow and the flow path is characterized by a curvilinear coordinate s along the fracture with the origin $s = 0$ at the perforation entry. The fluid flux along the fracture $q(s,t)$ can be given by Poiseuille's equation

$$q(s,t) = -\frac{w^3}{12\mu}\frac{\partial p}{\partial s} \tag{9}$$

in which w is the fracture opening width and μ is the dynamic viscosity of the fluid. The width w can be calculated based on the deformation of the solid medium as

$$w = (\mathbf{u}^+ - \mathbf{u}^-) \cdot \mathbf{n}^- \tag{10}$$

where $\mathbf{u}^+$ and $\mathbf{u}^-$ are the displacements on the fracture surfaces Γ_p^+ and Γ_p^- respectively and $\mathbf{n}^-$ is the outward normal vector for Γ_p^-.

In the absence of fluid leak-off, the continuity equation for fracture I can be written as

$$\frac{\partial w}{\partial t} + \frac{\partial q}{\partial s} = 0 \tag{11}$$

Combining Poiseuille's equation with the continuity equation, the Reynolds lubrication equation can be written as

$$\frac{\partial w}{\partial t} = \frac{\partial}{\partial s}\left(\frac{w^3}{12\mu}\frac{\partial p}{\partial s}\right) \tag{12}$$

The inlet boundary is

$$q|_{s=0} = q_I \tag{13}$$

If no lag exists at the fracture front, the boundary condition is

$$w_{tip} = 0, q_{tip} = 0 \tag{14}$$

where w_{tip} and q_{tip} are the fracture opening width and flow flux at the fracture front.

2.3 Fluid flow in the wellbore

The fluid flow in the wellbore is averaged over each cross-section and treated as one-dimensional flow. The mass conservation equations can be written as

$$Q_I = Q_0 - \sum_{J=1}^{I} 2hq_J, \quad I = 1, \ldots, N \tag{15}$$

$$Q_N = 0 \tag{16}$$

The balance of momentum for the fluid flow in the wellbore can be expressed in the form of Darcy–Weisbach equation as [33]

$$\Delta p_w = f(Re, e)\frac{D}{2a}\frac{\rho V|V|}{2} \tag{17}$$

in which p_w is the fluid pressure in the wellbore, Δp_w is the pressure loss along the wellbore with a length D, ρ is the density of the fluid and $V = Q/A$ is the cross-sectional averaged fluid velocity. The Darcy friction factor f is a function of the Reynolds number $Re = 2a\rho|V|/\mu$ and the roughness of the wellbore e. For laminar flow ($Re < 2000$), the friction factor $f = 64/Re$. For turbulent condition ($Re > 4000$), it can be obtained from Moody chart [34], or calculated by several approximation equations in the literature [35–37]. In the following simulations, we employ Balasius equation $f = 0.316/Re^{0.25}$ to calculate f for the turbulent flow, which is suited for relatively smooth pipes [33]. For critical regime ($2000 \le Re \le 4000$), a linear interpolation is adopted between laminar regime and turbulent regime.

If f is set to be zero, the pressure in the wellbore is constant, which can be used when the pressure loss in the wellbore is negligible or the pressure field is uniform in the fluid source region, which is the condition in magma chamber [1].

2.4 Perforation entry loss

When the fluid flows through a perforation cluster, a local pressure drop is induced by the entry friction of the perforations. The pressure drop at the perforation cluster of fracture I is denoted by $\Delta p_{entry,I}$, which is proportional to the square of the flux through the perforations and can be given by

$$\Delta p_{entry,I} = p_{w,I} - p_{e,I} = \varphi_{p,I} \cdot 2hq_I \cdot |2hq_I| \tag{18}$$

where $p_{w,I}$ is the pressure in the wellbore, $p_{e,I}$ is the pressure at the inlet of fracture I and $\varphi_{p,I}$ is the entry loss coefficient at the entry of fracture I. The entry loss coefficient φ_p depends on the fluid density, the number of perforations per cluster, the perforation diameter and the erosion condition of the perforations [38].

Limiting the number and diameter of perforations on the wellbore has been adopted as an effective technique to obtain simultaneous treatment of multiple zones, known as the "limited entry technique" [39,40]. The perforation entry loss can influence the partitioning of the fluid into fractures and then affect the propagation of multiple HFs.

3 Numerical discretization

3.1 XFEM formulation

XFEM is adopted to simulate the propagation of multiple HFs. It's proposed in 1999 [41] to model arbitrary crack growth and has been extended to a variety of applications [42]. Additional degrees of freedom (DOFs) are included to represent the discontinuity and singularity of the displacement fields. The approximation of the unknown displacement fields $\mathbf{u}^h(\mathbf{X})$ in XFEM is given by [43]

$$\begin{aligned}\mathbf{u}^h(\mathbf{X}) = &\sum_{\forall I} N_I(\mathbf{X})\mathbf{u}_I + \sum_{J \in S_H} N_J(\mathbf{X})\left[H(\varphi(\mathbf{X}))\right. \\ &\left.- H(\varphi(\mathbf{X}_J))\right]\mathbf{b}_J + \sum_{K \in S_T}\sum_m N_K(\mathbf{X}) \\ &\left[\Psi^m(\mathbf{X}) - \Psi^m(\mathbf{X}_K)\right]\mathbf{c}_K^m\end{aligned} \tag{19}$$

where S_T is the set of nodes located around the fracture tip, S_H is the set of nodes in elements completely crossed by the fracture (but not in S_T), $N_I(\mathbf{X})$ is the standard shape function and $\mathbf{u}_I$ is the standard DOF for node I, $\mathbf{b}_J$ and $\mathbf{c}_K^m$ are added DOFs for Heaviside and fracture tip enrichments respectively. The signed distance from the point $\mathbf{X}$ to the fracture surface is denoted as $\varphi(\mathbf{X})$ and $H(\cdot)$ is the Heaviside step function. A function collection Ψ^m is adopted to capture the asymptotic field near the fracture tip. If there's no lag between fluid front and fracture tip, the strong coupling between the fluid and the solid induces multi-scale behavior at the fracture tip [10]. The asymptotic displacement field behaves as r^λ and $1/2 \leq \lambda < 1$ for different propagation regimes. Gordeliy and Peirce [44] have suggested the following enrichment strategies for different regimes

$$\begin{aligned}&\{\Psi^m\}_{m=1}^4\\&= r^\lambda\{\sin(\lambda\theta), \cos(\lambda\theta), \sin(\lambda-2)\theta, \cos(\lambda-2)\theta\}\end{aligned} \tag{20}$$

where $\langle r, \theta\rangle$ is the polar coordinate system at the fracture tip. However, just as indicated in the introduction, the partitioning of the fluid into different fractures is constantly changing and the propagation regimes may change. It would be cumbersome to include different enrichments during the propagation process and so we only include $\lambda = 1/2$ in the simulation. Strictly speaking, the relationship $\lambda = 1/2$ is only valid for the conditions with a fluid lag or without a lag but toughness-dominated. In the simulation, we limit the tip enrichment within a quite small domain around the fracture tip and mainly take the advantage of the discontinuity representation of the enrichment. For relatively fine meshes, the numerical results show acceptable accuracy for different regimes, which can be referred to in Sect. 5.

For expression brevity, we combine the last two terms in Eq. (19) and rewrite it as

$$\mathbf{u}^h(\mathbf{X}) = \sum_{\forall I} N_I(\mathbf{X})\mathbf{u}_I + \sum_{J\in S} \Phi_J(\mathbf{X})\boldsymbol{\phi}_J \tag{21}$$

in which $S = \{S_H, 4\times S_T\}$, $\Phi_J(\mathbf{X})$ and $\boldsymbol{\phi}_J$ represent enriched shape function and enriched DOF, respectively.

Substituting displacement approximation Eq. (21) into the weak formulation of governing Eqs. (1)–(6), the discretized equations can be obtained as [45]

$$\begin{pmatrix}\mathbf{R}_1\\ \mathbf{R}_2\end{pmatrix} = \begin{bmatrix}\mathbf{K}^{uu} & \mathbf{K}^{u\phi}\\ \mathbf{K}^{\phi u} & \mathbf{K}^{\phi\phi}\end{bmatrix}\begin{pmatrix}\mathbf{u}\\ \boldsymbol{\phi}\end{pmatrix} - \begin{pmatrix}\mathbf{f}^u\\ \mathbf{f}^\phi\end{pmatrix} = \mathbf{0} \tag{22}$$

where $(\mathbf{u}\ \boldsymbol{\phi})^{\mathrm{T}}$ are standard DOFs and enriched DOFs, respectively, $\mathbf{K}^{uu}$, $\mathbf{K}^{u\phi}$, $\mathbf{K}^{\phi u}$ and $\mathbf{K}^{\phi\phi}$ are global stiffness matrixes by assembling the element stiffness matrixes and $\mathbf{f}^u$ and $\mathbf{f}^\phi$ are external forces. The superscripts "u" and "ϕ" correspond to standard DOFs and enriched DOFs respectively. The element stiffness matrix can be computed as

$$\begin{bmatrix}\mathbf{K}_e^{uu} & \mathbf{K}_e^{u\phi}\\ \mathbf{K}_e^{\phi u} & \mathbf{K}_e^{\phi\phi}\end{bmatrix} = \int_{\Omega_e}\left[\mathbf{B}^u\ \mathbf{B}^\phi\right]^{\mathrm{T}}\mathbf{C}\left[\mathbf{B}^u\ \mathbf{B}^\phi\right]\mathrm{d}\Omega \tag{23}$$

where Ω_e is the domain of the current element and the components of $\mathbf{B}^u$ and $\mathbf{B}^\phi$ are

$$\mathbf{B}_I^u = \begin{bmatrix}N_{I,x} & 0\\ 0 & N_{I,y}\\ N_{I,y} & N_{I,x}\end{bmatrix},\quad \mathbf{B}_I^\phi = \begin{bmatrix}\Phi_{I,x} & 0\\ 0 & \Phi_{I,y}\\ \Phi_{I,y} & \Phi_{I,x}\end{bmatrix} \tag{24}$$

Within the element containing the fracture, $\Phi_{I,x}$ and $\Phi_{I,y}$ are discontinuous and subdomain integration method [41] is adopted to calculate the discontinuous integral. The external forces for each element are given as

$$\mathbf{f}_e^u = \int_{\Gamma_{te}}\mathbf{N}^{\mathrm{T}}\cdot\bar{\mathbf{t}}\,\mathrm{d}\Gamma,\ \mathbf{f}_e^\phi = \int_{\Gamma_{pe}^+ + \Gamma_{pe}^-}\boldsymbol{\Phi}^{\mathrm{T}}\cdot(-p\mathbf{n})\mathrm{d}\Gamma \tag{25}$$

where Γ_{te}, Γ_{pe}^+ and Γ_{pe}^- are the boundaries within the current element and the components of $\mathbf{N}$ and $\boldsymbol{\Phi}$ are given by

$$\mathbf{N}_I = \begin{bmatrix}N_I & 0\\ 0 & N_I\end{bmatrix},\ \boldsymbol{\Phi}_I = \begin{bmatrix}\Phi_I & 0\\ 0 & \Phi_I\end{bmatrix} \tag{26}$$

3.2 Discretization of the fluid flow equations in fractures

Finite volume method (FVM) is adopted to model the fluid flow in fractures. The fracture in one solid element is discretized as one fluid cell. Firstly we focus on the discretization of a single fracture and then integrate the discretization for all fractures to obtain the final discretization equations.

Assume that the flow in one single fracture with an inlet flux q_{inlet} is discretized by n fluid elements as shown in Fig. 2. The pressure and the opening width at the midpoint of the ith fluid element are denoted as p_i and w_i, respectively. Two endpoints of the ith fluid element are denoted as $i-1/2$ and $i+1/2$. The approximation of the pressure along a fracture is given by the linear Lagrange interpolation as follows:

$$p(s,t) = \sum_{i=1}^n L_i(s)p_i(t) \tag{27}$$

where for $i = 1$,

$$L_1(s) = \begin{cases}\frac{s_2-s}{s_2-s_1}, & \text{if } s_{1/2}\leq s < s_2\\ 0, & \text{else}\end{cases} \tag{28}$$

Fig. 2 Discretization of the fluid flow in a HF

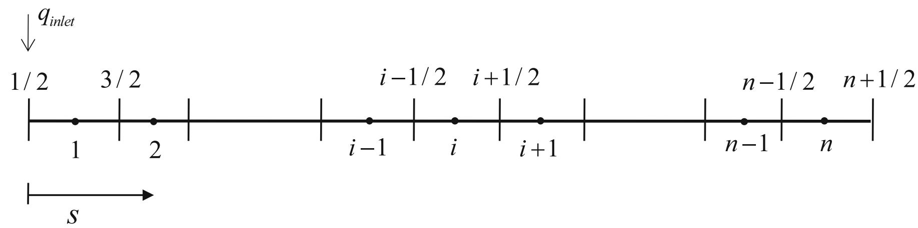

and for $2 \leq i \leq n-1$,

$$L_i(s) = \begin{cases} \frac{s-s_{i-1}}{s_i-s_{i-1}}, & \text{if} \begin{cases} s_{i-3/2} \leq s < s_i, & \text{if } i=2 \\ s_{i-1} \leq s < s_i, & \text{else} \end{cases} \\ \frac{s_{i+1}-s}{s_{i+1}-s_i}, & \text{if} \begin{cases} s_i \leq s < s_{i+3/2}, & \text{if } i=n-1 \\ s_i \leq s < s_{i+1}, & \text{else} \end{cases} \\ 0, & \text{else} \end{cases} \tag{29}$$

and for $i = n$,

$$L_n(s) = \begin{cases} \frac{s-s_{n-1}}{s_n-s_{n-1}}, & \text{if } s_{n-1} \leq s < s_{n+1/2} \\ 0, & \text{else} \end{cases} \tag{30}$$

The fracture opening width can be computed by Eqs. (10) and (21) as

$$\begin{aligned} w(s,t) = w\left(s(\mathbf{X}),t\right) &= \left[\mathbf{u}^h(\mathbf{X}^+) - \mathbf{u}^h(\mathbf{X}^-)\right] \cdot \mathbf{n}^- \\ &= \sum_{J \in S} \left[\Phi_J(\mathbf{X}^+) - \Phi_J(\mathbf{X}^-)\right] \boldsymbol{\phi}_J \cdot \mathbf{n}^- \end{aligned} \tag{31}$$

We just calculate the width at the midpoints by Eq. (31) and approximate w along the fracture by the linear Lagrange interpolation similar to Eq. (27) with $w_{n+1/2} = 0$ included.

Integrating the Reynolds equation (12) over the ith fluid cell and approximating the fluxes with the central difference and approximating the derivative versus time using the backward difference, for $2 \leq i \leq n-1$ we can get

$$\begin{aligned} &\int_{s_{i-1/2}}^{s_{i+1/2}} \frac{w - w^0}{\Delta t} \mathrm{d}s \\ &= \frac{w_{i+1/2}^3}{12\mu} \frac{p_{i+1}-p_i}{s_{i+1}-s_i} - \frac{w_{i-1/2}^3}{12\mu} \frac{p_i - p_{i-1}}{s_i - s_{i-1}} \end{aligned} \tag{32}$$

in which Δt is the time increment and the quantities in the previous time step are marked with the superscript "0" and the other quantities are in the current time step. Substituting the approximation of w into Eq. (32) and rearranging the terms, we can obtain

$$A_{i,i-1} p_{i-1} + A_{ii} p_i + A_{i,i+1} p_{i+1} - d_i = 0, 2 \leq i \leq n-1 \tag{33}$$

where

$$\begin{aligned} A_{i,i-1} &= \frac{w_{i-1/2}^3}{12\mu(s_i - s_{i-1})}, \ A_{ii} = -\frac{w_{i-1/2}^3}{12\mu(s_i - s_{i-1})} \\ &- \frac{w_{i+1/2}^3}{12\mu(s_{i+1}-s_i)}, \ A_{i,i+1} = \frac{w_{i+1/2}^3}{12\mu(s_{i+1}-s_i)} \end{aligned} \tag{34}$$

and

$$\begin{aligned} d_i = \frac{1}{\Delta t} \Bigg[&\left(s_{i+1/2} - s_{i-1/2}\right) \cdot \frac{w_{i-1/2} + 2w_i + w_{i+1/2}}{4} \\ &- \left(s_{i+1/2}^0 - s_{i-1/2}^0\right) \cdot \frac{w_{i-1/2}^0 + 2w_i^0 + w_{i+1/2}^0}{4} \Bigg] \end{aligned} \tag{35}$$

$$\begin{aligned} w_{i-1/2} &= L_{i-1}(s_{i-1/2}) w_{i-1} + L_i(s_{i-1/2}) w_i, \ w_{i+1/2} \\ &= L_i(s_{i+1/2}) w_i + L_{i+1}(s_{i+1/2}) w_{i+1} \end{aligned} \tag{36}$$

For $i = 1$, including the inlet flux boundary Eq. (13) we can obtain

$$A_{11} p_1 + A_{12} p_2 - d_1 = 0 \tag{37}$$

with

$$A_{11} = -\frac{w_{3/2}^3}{12\mu(s_2 - s_1)}, A_{12} = \frac{w_{3/2}^3}{12\mu(s_2 - s_1)} \tag{38}$$

and

$$d_1 = \frac{1}{\Delta t} \left[\left(s_{3/2} - s_{1/2}\right) \cdot w_1 - \left(s_{3/2}^0 - s_{1/2}^0\right) \cdot w_1^0 \right] - q_{inlet} \tag{39}$$

For $i = n$, including the fracture front boundary conditions (14) we can obtain

$$A_{n,n-1} p_{n-1} + A_{nn} p_n - d_n = 0 \tag{40}$$

with

$$A_{n,n-1} = \frac{w_{n-1/2}^3}{12\mu(s_n - s_{n-1})}, A_{nn} = -\frac{w_{n-1/2}^3}{12\mu(s_n - s_{n-1})} \tag{41}$$

and

$$d_n = \frac{1}{\Delta t}\left[\left(s_{n+1/2} - s_{n-1/2}\right)\cdot\frac{w_{n-1/2}+2w_n}{4} - \left(s^0_{n+1/2} - s^0_{n-1/2}\right)\cdot\frac{w^0_{n-1/2}+2w^0_n}{4}\right] \tag{42}$$

Combining Eqs. (33), (37) and (40), the discretization formulation of the fluid flow equation can be given by

$$\sum_j A_{ij}p_j - d_i = 0, \begin{cases} j = 1, 2 & \text{if } i = 1 \\ j = n-1, n & \text{if } i = n \\ j = i-1, i, i+1 & \text{else} \end{cases} \tag{43}$$

or in matrix form as

$$\mathbf{A}\left(\mathbf{w}(\boldsymbol{\phi})\right)\cdot\mathbf{p} - \mathbf{d}\left(\mathbf{w}(\boldsymbol{\phi}), q_{inlet}\right) = \mathbf{0} \tag{44}$$

where $\mathbf{A}$ is a function of the widths of midpoints $\mathbf{w}$, $\mathbf{d}$ is a function of $\mathbf{w}$ and the inlet flux q_{inlet}. As shown in Eq. (31), $\mathbf{w}$ can be further written as $\mathbf{w}(\boldsymbol{\phi})$.

Next, we will integrate the discretization for all fractures. To distinguish different fractures, the quantities related to fracture I are marked with subscript "I". The pressure and the width are respectively denoted as p_{Ii} and w_{Ii} at the midpoint of the ith fluid element on fracture I.

Define $\mathbf{p}_I = \left[p_{I1}, p_{I2}, \ldots, p_{In_I}\right]^{\mathrm{T}}$ and $\mathbf{w}_I = [w_{I1}, w_{I2}, \ldots, w_{In_I}]^{\mathrm{T}}$ for the midpoints on fracture I and define $\mathbf{A}_I$, $\mathbf{d}_I$ correspondingly. Define $\mathbf{p}_f = \left[(\mathbf{p}_1)^{\mathrm{T}}, (\mathbf{p}_2)^{\mathrm{T}}, \ldots, (\mathbf{p}_N)^{\mathrm{T}}\right]^{\mathrm{T}}$, $\mathbf{w}_f = \left[(\mathbf{w}_1)^{\mathrm{T}}, (\mathbf{w}_2)^{\mathrm{T}}, \ldots, (\mathbf{w}_N)^{\mathrm{T}}\right]^{\mathrm{T}}$ and $\mathbf{q} = [q_1, q_2, \ldots, q_N]^{\mathrm{T}}$, $\mathbf{d}_f = \left[(\mathbf{d}_1)^{\mathrm{T}}, (\mathbf{d}_2)^{\mathrm{T}}, \ldots, (\mathbf{d}_N)^{\mathrm{T}}\right]^{\mathrm{T}}$ for all the N fractures. Finally, the discretization formulation for all HFs can be assembled as

$$\mathbf{R}_3\left(\boldsymbol{\phi}, \mathbf{p}_f, \mathbf{q}\right) = \mathbf{A}_f\left(\mathbf{w}_f(\boldsymbol{\phi})\right)\cdot\mathbf{p}_f - \mathbf{d}_f\left(\mathbf{w}_f(\boldsymbol{\phi}), \mathbf{q}\right) = \mathbf{0} \tag{45}$$

with

$$\mathbf{A}_f = \begin{bmatrix} \mathbf{A}_1 & & & \\ & \mathbf{A}_2 & & \\ & & \ddots & \\ & & & \mathbf{A}_N \end{bmatrix} \tag{46}$$

3.3 Discretization of fluid flow equations in the wellbore

The pressure at the inlet of fracture I $p_{e,I}$ can be approximated by the pressure at the midpoint of the first fluid cell p_{I1}. Then Eq. (18) can be rewritten as

$$p_{w,I} \approx p_{I1} + 4\varphi_{p,I}h^2 q_I\cdot|q_I| \tag{47}$$

For the flow in the wellbore between the Ith and $(I+1)$th fractures, the pressure loss can be given by

$$p_{w,I} - p_{w,I+1} = \left(p_{I1} + 4\varphi_{p,I}h^2 q_I\cdot|q_I|\right) - \left(p_{I+1,1} + 4\varphi_{p,I+1}h^2 q_{I+1}\cdot|q_{I+1}|\right), \quad 1 \le I \le N-1 \tag{48}$$

Substituting $Re = 2a\rho|V|/\mu$ and $V = Q/(\pi a^2)$ into Eq. (17) and combining with Eq. (15), we can obtain

$$\left(p_{I1} + 4\varphi_{p,I}h^2 q_I\cdot|q_I|\right) - \left(p_{I+1,1} + 4\varphi_{p,I+1}h^2 q_{I+1}\cdot|q_{I+1}|\right) - \frac{\rho D_I}{4\pi^2 a^5} f\left(\frac{2\rho\left|Q_0 - \sum_{J=1}^{I}2hq_J\right|}{\pi\mu a}, e\right)\cdot\left(Q_0 - \sum_{J=1}^{I}2hq_J\right)\left|Q_0 - \sum_{J=1}^{I}2hq_J\right| = 0, 1 \le I \le N-1 \tag{49}$$

The above $N-1$ equations are written as

$$\mathbf{R}_4\left(\mathbf{p}_f, \mathbf{q}\right) = 0 \tag{50}$$

Substituting Eqs. (15) into (16) we can obtain

$$Q_0 - \sum_{J=1}^{N}2hq_J = 0 \tag{51}$$

or in a matrix form

$$\mathbf{R}_5(\mathbf{q}) = 0 \tag{52}$$

4 Solving schemes

For a given time increment Δt, the solution of the coupled equations includes the propagation lengths of all HFs $\Delta\mathbf{l}$, the values of standard DOFs $\mathbf{u}$ and enriched DOFs $\boldsymbol{\phi}$ for the solid nodes, the pressures on the midpoints of all fluid cells $\mathbf{p}_f$ and the inlet fluxes for all HFs $\mathbf{q}$. The propagation lengths $\Delta\mathbf{l}$ are coupled with the other unknowns in a complex form and it's solved separately. There are two nested loops in a time step. The outer loop is an iteration for the propagation lengths with secant iteration method and the inner loop is Newton's iteration to solve the unknowns $\left(\mathbf{u}, \boldsymbol{\phi}, \mathbf{p}_f, \mathbf{q}\right)$.

4.1 Newton's iteration

For a set of specified fracture lengths, the discretization equations to be solved are the combination of solid deformation equations Eq. (22), fracture flow equations Eq. (45), wellbore flow equations Eqs. (50) and (52), which can be combined as

$$\mathbf{R}\left(\mathbf{u},\boldsymbol{\phi},\mathbf{p}_f,\mathbf{q}\right)=\begin{bmatrix}\mathbf{R}_1\left(\mathbf{u},\boldsymbol{\phi}\right)\\ \mathbf{R}_2\left(\mathbf{u},\boldsymbol{\phi},\mathbf{p}_f\right)\\ \mathbf{R}_3\left(\boldsymbol{\phi},\mathbf{p}_f,\mathbf{q}\right)\\ \mathbf{R}_4\left(\mathbf{p}_f,\mathbf{q}\right)\\ \mathbf{R}_5\left(\mathbf{q}\right)\end{bmatrix}=\mathbf{0} \tag{53}$$

which are fully coupled and nonlinear. Newton's iteration is used to solve these equations. Assume $\left(\mathbf{u}_\alpha,\boldsymbol{\phi}_\alpha,\mathbf{p}_{f,\alpha},\mathbf{q}_\alpha\right)$ are the values at the α th iteration and then

$$\begin{pmatrix}\mathbf{u}_{\alpha+1}\\ \boldsymbol{\phi}_{\alpha+1}\\ \mathbf{p}_{f,\alpha+1}\\ \mathbf{q}_{\alpha+1}\end{pmatrix}=\begin{pmatrix}\mathbf{u}_{\alpha}\\ \boldsymbol{\phi}_{\alpha}\\ \mathbf{p}_{f,\alpha}\\ \mathbf{q}_{\alpha}\end{pmatrix} -\mathbf{K}^{-1}\left(\mathbf{u}_\alpha,\boldsymbol{\phi}_\alpha,\mathbf{p}_{f,\alpha},\mathbf{q}_\alpha\right)\cdot\mathbf{R}\left(\mathbf{u}_\alpha,\boldsymbol{\phi}_\alpha,\mathbf{p}_{f,\alpha},\mathbf{q}_\alpha\right) \tag{54}$$

where the system Jacobian matrix $\mathbf{K}$ is given in the following formulation:

$$\mathbf{K}=\frac{\partial\mathbf{R}}{\partial\left(\mathbf{u},\boldsymbol{\phi},\mathbf{p}_f,\mathbf{q}\right)}=\begin{Bmatrix}\mathbf{K}^{uu} & \mathbf{K}^{u\phi} & & \\ \mathbf{K}^{\phi u} & \mathbf{K}^{\phi\phi} & -\frac{\partial\mathbf{f}^{\phi}}{\partial\mathbf{p}_f} & \\ & \frac{\partial\mathbf{R}_3}{\partial\boldsymbol{\phi}} & \mathbf{A}_f & -\frac{\partial\mathbf{d}_f}{\partial\mathbf{q}}\\ & & \frac{\partial\mathbf{R}_4}{\partial\mathbf{p}_f} & \frac{\partial\mathbf{R}_4}{\partial\mathbf{q}}\\ & & & \frac{\partial\mathbf{R}_5}{\partial\mathbf{q}}\end{Bmatrix} \tag{55}$$

$$\mathbf{f}_e^{\phi}=\int_{\Gamma_{pe}^{+}+\Gamma_{pe}^{-}}\boldsymbol{\Phi}^{\mathrm{T}}\cdot\left[-\left(\sum_{i=1}^{n_I}L_{Ii}p_{Ii}\right)\mathbf{n}\right]\mathrm{d}\Gamma \tag{56}$$

where L_{Ii} is the Lagrange interpolation function for the ith node on fracture I. The derivative with respect to p_{Mk} can be given as

$$\frac{\partial\mathbf{f}_e^{\phi}}{\partial p_{Mk}}=\begin{cases}\int_{\Gamma_{pe}^{+}+\Gamma_{pe}^{-}}\boldsymbol{\Phi}^{\mathrm{T}}\cdot\left(-L_{Ik}\mathbf{n}\right)\mathrm{d}\Gamma, & \text{if } M=I\\ \mathbf{0}, & \text{else}\end{cases} \tag{57}$$

As the components of $\partial\mathbf{R}_3/\partial\boldsymbol{\phi}$, the derivative of Eq. (43) for the ith fluid cell on fracture I with respect to ϕ_m can be written as

$$\frac{\partial R_{3,Ii}}{\partial\phi_m}=\sum_j\left[\sum_k\frac{\partial A_{I,ij}}{\partial w_{I,k}}\frac{\partial w_{I,k}}{\partial\phi_m}p_{I,j}\right] -\sum_k\frac{\partial d_{I,i}}{\partial w_{I,k}}\frac{\partial w_{I,k}}{\partial\phi_m},\ \begin{cases}j,k=1,2 & \text{if } i=1\\ j,k=n_I-1,n_I & \text{if } i=n_I\\ j,k=i-1,i,i+1 & \text{else}\end{cases} \tag{58}$$

where $R_{3,Ii}$ represents Eq. (43) for the ith fluid cell on fracture I.

For $-\partial\mathbf{d}_f/\partial\mathbf{q}$, from Eq. (39) we can obtain

$$\frac{\partial d_{Ii}}{\partial q_M}=\begin{cases}-1, & \text{if } i=1 \text{ and } M=I\\ 0, & \text{else}\end{cases} \tag{59}$$

We can get $\partial\mathbf{R}_4/\partial\mathbf{p}_f$ and $\partial\mathbf{R}_4/\partial\mathbf{q}$ from the derivative of Eq. (49) as

$$\frac{\partial R_{4,I}}{\partial p_{Mk}}=\begin{cases}1, & \text{if } k=1 \text{ and } M=I\\ -1, & \text{if } k=1 \text{ and } M=I+1\\ 0, & \text{else}\end{cases} \tag{60}$$

$$\frac{\partial R_{4,I}}{\partial q_M}=\begin{cases}-\frac{\rho D_I}{4\pi^2a^5}\left[\frac{\partial f}{\partial q_M}\cdot\left(Q_0-\sum_{J=1}^{I}2hq_J\right)-4fh\right]\cdot\left|Q_0-\sum_{J=1}^{I}2hq_J\right|, & \text{if } 1\le M<I\\ 8\varphi_{p,I}h^2\left|q_I\right|-\frac{\rho D_I}{4\pi^2a^5}\left[\frac{\partial f}{\partial q_M}\cdot\left(Q_0-\sum_{J=1}^{I}2hq_J\right)-4fh\right]\cdot\left|Q_0-\sum_{J=1}^{I}2hq_J\right|, & \text{if } M=I\\ -8\varphi_{p,I+1}h^2\left|q_{I+1}\right|, & \text{if } M=I+1\\ 0, & \text{else}\end{cases} \tag{61}$$

The terms in Eq. (55) are assembled by the components computed on the solid and fluid elements.

Denoting the fracture index in the current solid element as I and substituting Eq. (27) into the second equation of Eq. (25), we can obtain the external force corresponding to the enriched DOFs as

The derivative $\partial\mathbf{R}_5/\partial\mathbf{q}$ can be obtained by

$$\frac{\partial R_{5,1}}{\partial q_M}=-2h \tag{62}$$

where $R_{5,1}$ is the sole component of $\mathbf{R}_5$.

The convergence criterion for Newton's iteration is

$$\max\left(\frac{\|\mathbf{u}_{\alpha+1}-\mathbf{u}_{\alpha}\|_2}{\|\mathbf{u}_{\alpha}\|_2}, \frac{\|\boldsymbol{\phi}_{\alpha+1}-\boldsymbol{\phi}_{\alpha}\|_2}{\|\boldsymbol{\phi}_{\alpha}\|_2}, \frac{\|\mathbf{p}_{f,\alpha+1}-\mathbf{p}_{f,\alpha}\|_2}{\|\mathbf{p}_{f,\alpha}\|_2}, \frac{\|\mathbf{q}_{\alpha+1}-\mathbf{q}_{\alpha}\|_2}{\|\mathbf{q}_{\alpha}\|_2}\right) < \varepsilon \tag{63}$$

The permissible error ε is adopted as 10^{-5} in the simulations.

4.2 Secant iteration for fracture lengths

For a prescribed time increment Δt, the propagation lengths are the unknowns to be found. For a single fracture, secant iteration can be adopted based on the fact that the equivalent SIF K_{eq} is always equal to the critical value K_{Ic}. The equivalent SIF K_{eq} can be regarded as a function of the fracture propagation length Δl and the difference between K_{eq} and K_{Ic} can be written as

$$g(\Delta l) = K_{eq}(\Delta l) - K_{Ic} = 0 \tag{64}$$

Secant iteration is a two-step iterative algorithm and two initial estimated values, Δl^1 and Δl^2, should be prescribed. Then Δl^3 for the next iteration step can be given as

$$\Delta l^3 = \Delta l^2 - \frac{g\left(\Delta l^2\right)\left(\Delta l^2 - \Delta l^1\right)}{g\left(\Delta l^2\right) - g\left(\Delta l^1\right)} \tag{65}$$

where the superscript represents the iteration step. The iteration continues until the convergence condition is satisfied by

$$\frac{\left|K_{eq}\left(\Delta l^3\right) - K_{Ic}\right|}{|K_{Ic}|} < \varepsilon \tag{66}$$

where ε is set to be 10^{-4} in the iteration for the length and may be increased to 10^{-3} if too many iterations are needed.

For the propagation of multiple HFs, fractures can interact with each other and the equivalent SIF for fracture I, $K_{eq,I}(\Delta l_1, \Delta l_2, \ldots, \Delta l_N)$, is a function of propagation lengths of all fractures. Newton's iteration or quasi-Newton's iteration can be adopted to get faster convergence. However, in both iteration methods the derivatives of $K_{eq,I}$ with respect to Δl_J, $1 \le I \le N$, $1 \le J \le N$, need to be calculated by numerical method, which requires large computing resources. So in our simulation, the secant iteration is adopted for each fracture and it also reveals acceptable convergence efficiency.

4.3 Computation of SIFs

The secant iteration for fracture length is based on the SIFs and the extraction of SIFs with good accuracy is the guarantee of convergence. Here, interaction integral [46–48] is adopted to extract the SIFs. The integral domain S is shown in Fig. 3,

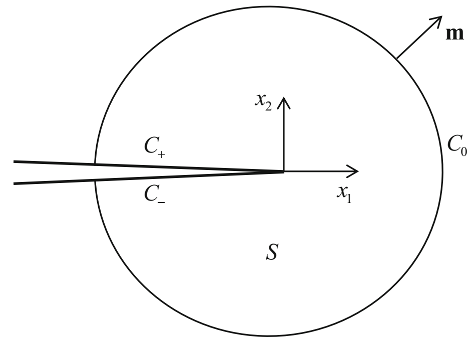

Fig. 3 The domain for interaction integral

where C_0 is the outer boundary of the domain. Assume the fracture in the domain is straight and C_+ and C_- are fracture surfaces inside the integral domain. The outward unit normal vector on the boundary $C = C_0 + C_+ + C_-$ is denoted as $\mathbf{m}$. The local coordinate system with the origin located on the fracture front and x_1 axis tangential to the fracture is denoted as $\langle x_1, x_2\rangle$. The interaction integral can be given as

$$I^m = \int_S \left[\sigma_{ij}\frac{\partial u_i^m}{\partial x_1} + \sigma_{ij}^m \frac{\partial u_i}{\partial x_1} - W\delta_{1j}\right]\frac{\partial \beta}{\partial x_j}\mathrm{d}S + \int_{C_+ + C_-} p\frac{\partial u_2^m}{\partial x_1}\beta m_2 \mathrm{d}C,\ \ m = I, II \tag{67}$$

where $\left(\sigma_{ij}, \varepsilon_{ij}, u_i\right)$ are the fields of the present state and $\left(\sigma_{ij}^m, \varepsilon_{ij}^m, u_i^m\right)$ are the theoretical asymptotic fields for the crack with mode $m = I, II$. The function $W = \sigma_{ij}\varepsilon_{ij}^m = \sigma_{ij}^m\varepsilon_{ij}$ and β is a weight function which equals to 1 at the fracture front and vanishes on the outer boundary C_0. SIFs can be given by

$$K_m = \frac{E'}{2}I^m, \quad m = I, II \tag{68}$$

where $E' = E/\left(1-\nu^2\right)$ for plane strain model.

5 Verification

Numerical examples are given to verify the proposed algorithm in this paper for the propagation of one HF and the initiation of two HFs. In the first example, the numerical results are compared with the analytical and asymptotic solutions in the literatures for the propagation of one single HF. For a model containing two HFs without stress interaction and driven by inviscid fluid we can derive the fluid partitioning analytically for the fracture initiating procedure. The numerical results are compared with the analytical solutions considering different entry loss coefficients. The characteristic dimensions of the model are much larger than the fracture lengths, which can be considered as approximation of the propagation in an infinite domain. Quadrilateral elements are adopted. Fine meshes are generated in the propagation regions and relatively coarse meshes are adopted far away from these regions.

5.1 Propagation of one HF

The analytical and semi-analytical solutions for the propagation of one plane-strain HF can be found in [8]. A dimensionless toughness $\mathcal{K}_m$ is defined to characterize the propagation regimes as follows:

$$\mathcal{K}_m = \frac{K'}{\left(E'^3\mu' q\right)^{1/4}} \tag{69}$$

where $K' = 8K_{Ic}/\sqrt{2\pi}$, $\mu' = 12\mu$ and $q = 2q_{inlet}$. If $\mathcal{K}_m = 0$, the solution is called M-vertex solution and if $\mathcal{K}_m \to \infty$, it's called K-vertex solution. For the range $\mathcal{K}_m < 1$, the propagation is in viscosity-dominated regime, which means most of the energy is dissipated by the viscous flow in the fracture. The solution for viscosity-dominated regime can be approximated by the M-vertex solution [8]. In contrast, for the range $\mathcal{K}_m > 4$, the propagation is in toughness-dominated regime, which means most of the energy is dissipated by the fracturing of the solid medium. The first-order K-vertex solution can be adopted to approximate this regime. The range $1 \leq \mathcal{K}_m \leq 4$ is in transition regime.

The geometry dimensions are shown in Fig. 4. Only half of the model is depicted. The parameters for two cases are shown in Table 1. The dimensionless toughness $\mathcal{K}_m$ is 0.685 for Case 1, which is viscosity-dominated regime and it's 6.85 for Case 2, which is toughness-dominated regime. 9010 quadrilateral elements are adopted to discretize the model. The initial time increments for viscosity-dominated regime and toughness-dominated regime are 0.02 and 0.1 s, respectively. In numerical simulation, an initial fracture with a short length should be given in advance and the initial conditions are prescribed with theoretical solutions. The numerical results for the two different regimes are shown in Figs. 5 and 6. The evolutions of the fracture length and inlet pressure are compared with the theoretical solutions, which are in good agreement. For both regimes, the fracture lengths varies with time in the order of $2/3$ and the inlet pressures varies in the order of $-1/3$.

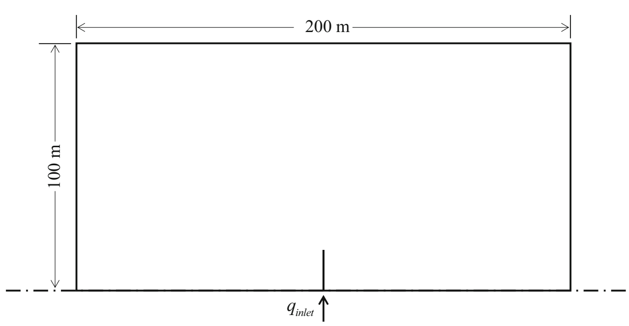

Fig. 4 Propagation of one HF

Theoretical and numerical pressure profiles along the fracture for both regimes are depicted in Fig. 7. The profiles are extracted from the results when the fracture reaches the length of 10m. The position s along the fracture is scaled by the fracture length and the pressure is scaled by the inlet pressure. We can see that the numerical pressure profiles agree well with the theoretical profiles for both regimes except that the theoretical pressure for viscosity-dominated regime is singular near the fracture tip and so relatively larger errors exist for numerical results near the tip. For toughness-dominated regime, the pressure is nearly constant along the fracture just as expected.

In order to demonstrate the performance of the secant iteration for fracture length, the numbers of secant iterations versus the time steps for both regimes are shown in Fig. 8 for the first 50 steps. The convergence of the secant algorithm can be obtained mostly within four iterations.

5.2 Initiation of two HFs with different lengths

In this example, we investigate the influence of the perforation entry loss on fluid partitioning. Consider two short fractures with different initial half lengths of 1.2 and 1.0 m, as shown in Fig. 9. The two fractures are located with a distance of $D = 100$ m, which is much larger than their lengths and so the interaction stress between them can be neglected. They are interconnected by a wellbore and inviscid fluid is pumped into them. Pressure loss in the wellbore is also neglected. We focus on the process before fractures start to propagate, which is similar to the initiation of two HFs. The other parameters include $E = 20$ GPa, $\nu = 0.2$, $Q_0 = 0.002$ m^3/s, $h = 1$ m and the initial pressure $p_0 = 1$ MPa. There are 11,547 quadrilateral elements meshed and the time increment is 0.01s. In view of the

Table 1 Parameters for different propagation regimes

	E (GPa)	ν	K_{Ic} (MPa $\sqrt{\text{m}}$)	μ (Pa s)	q_{inlet} (m^2/s)	$\mathcal{K}_m$
Case 1	10	0.2	4.9	1.0	0.01	0.685
Case 2	10	0.2	4.9	0.001	0.001	6.85

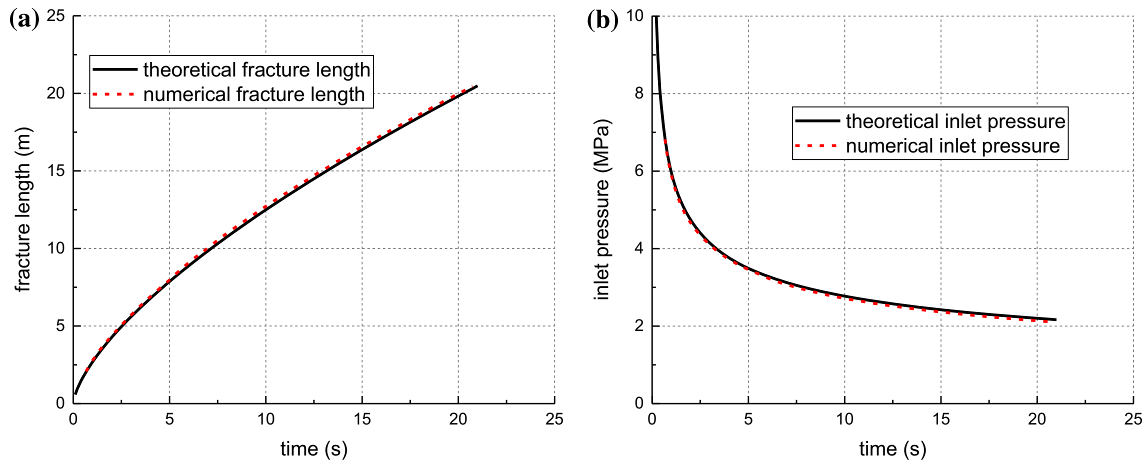

Fig. 5 Simulation results for viscosity-dominated regime: **a** evolution of the fracture length. **b** Evolution of the inlet pressure

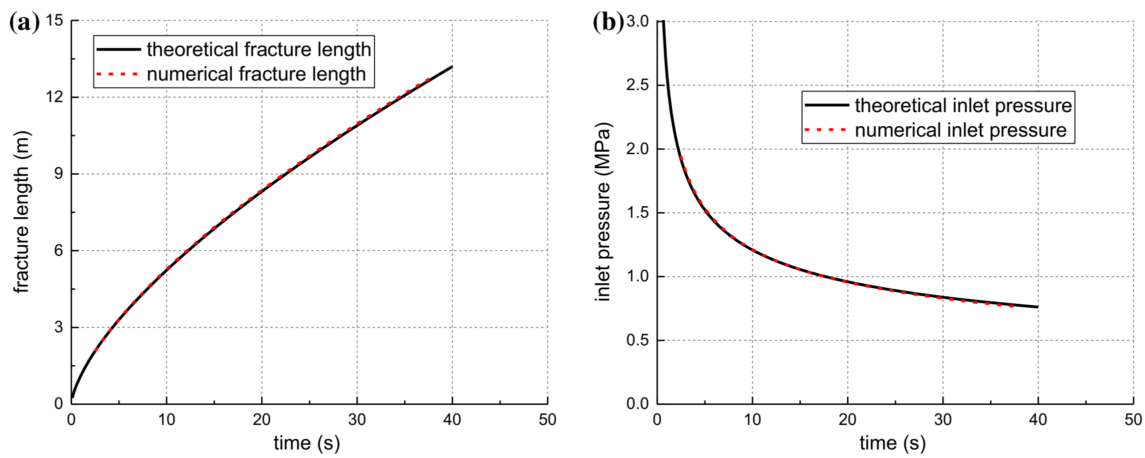

Fig. 6 Simulation results for toughness-dominated regime: **a** evolution of the fracture length. **b** Evolution of the inlet pressure

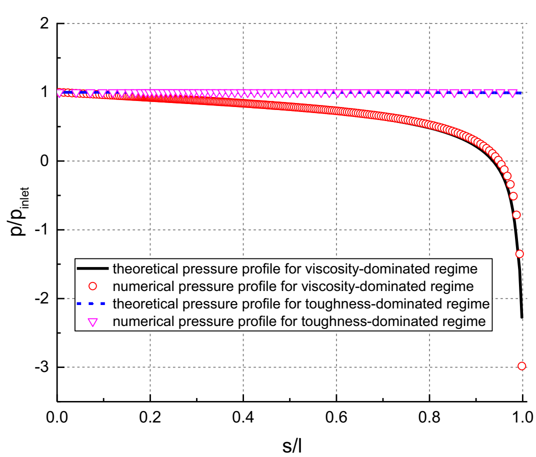

Fig. 7 Theoretical and numerical pressure profiles along the fracture for viscosity-dominated and toughness-dominated regimes, respectively

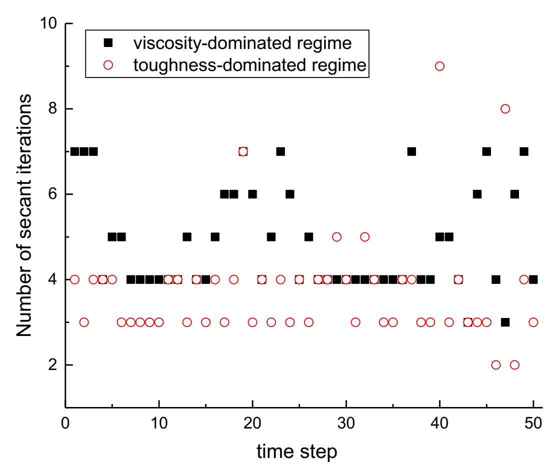

Fig. 8 Numbers of secant iterations versus time steps for the propagation of one single fracture in viscosity-dominated and toughness-dominated regimes

assumptions that the stress interaction and fluid viscosity are neglected, this problem is solved analytically as given in "Appendix".

Four different entry loss coefficients $\varphi_p = 10^4, 10^5, 10^6, 10^7$ MPa s^2/m^6 are considered. The evolution of inlet fluxes into different fractures by theoretical analysis and numerical simulation is shown in Fig. 10. Just as the same as the analytical analysis given in "Appendix", the inlet fluxes for the two fractures are initially equal and they will evolve to different steady values. The steady values are independent of the entry loss coefficients. However, the critical time defined in "Appendix" $t_c = 4c_1c_2\varphi_p h Q_0/(c_1+c_2)$ is proportional to φ_p. As the increase of φ_p, more time is required for the inlet fluxes to reach the steady values, which means in a relatively long period of time the fluid is nearly evenly partitioned. Perforation entry loss can act as a counterbalance effect to non-uniform fluid partitioning. If too much fluid flows into one fracture, much more pressure will be lost at the inlet, which decreases the driving force for that fracture and then the inlet flux decreases accordingly.

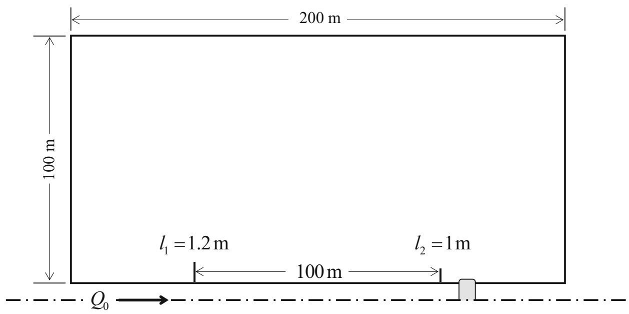

Fig. 9 Initiation of two HFs with different initial lengths

6 Study of simultaneous propagation of multiple HFs

6.1 Model description and scale estimation

When multiple HFs are driven to propagate simultaneously as shown in Fig. 11, some fractures may grow faster than others, which is not desired in engineering application. The propagation path may be affected by several factors, including the

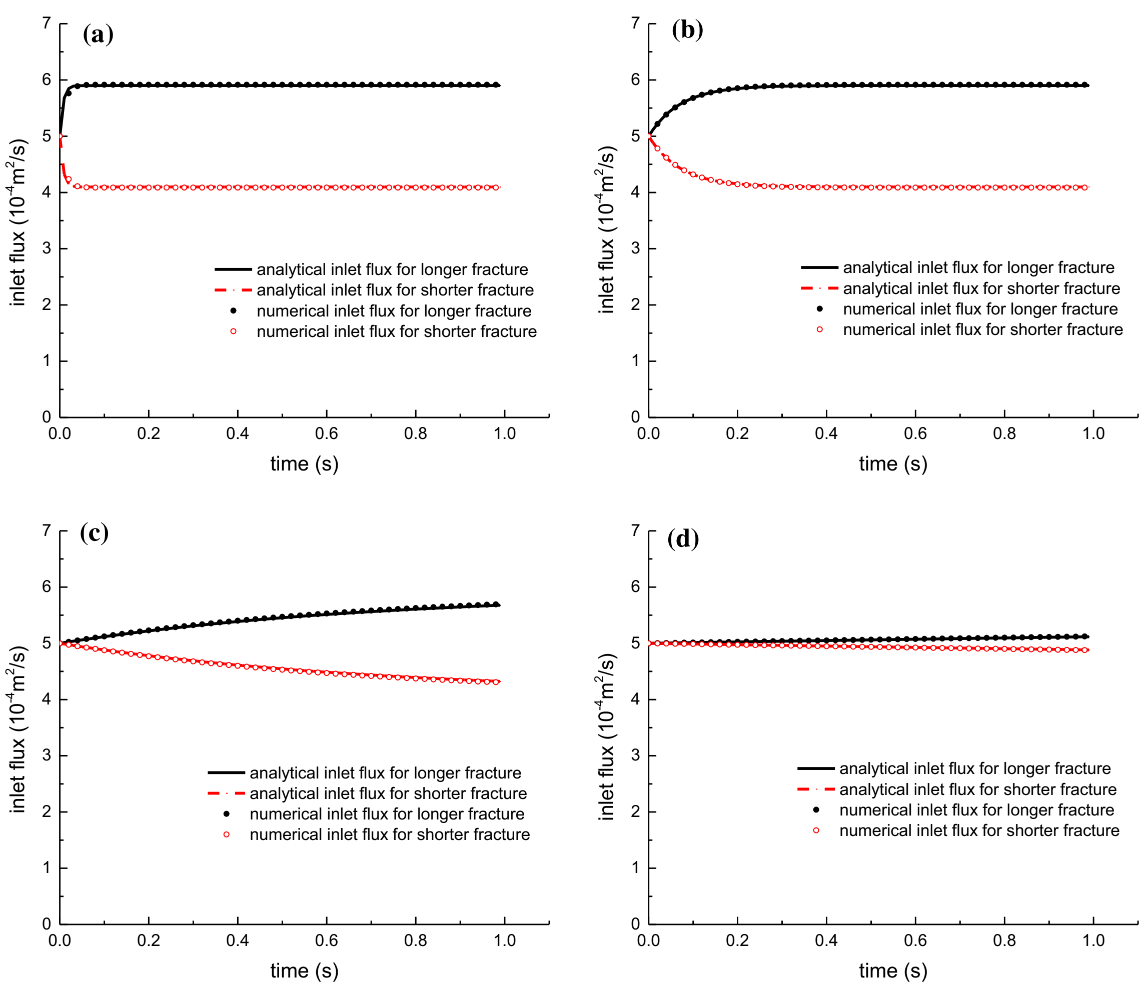

Fig. 10 Evolution of analytical and numerical inlet fluxes into fractures for different entry loss coefficients: **a** $\varphi_p = 10^4$ MPa s^2/m^6, **b** $\varphi_p = 10^5$ MPa s^2/m^6, **c** $\varphi_p = 10^6$ MPa s^2/m^6, **d** $\varphi_p = 10^7$ MPa s^2/m^6

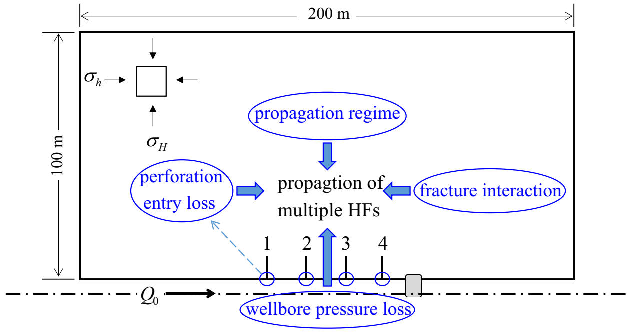

Fig. 11 Simultaneous propagation of multiple HFs

propagation regime, the stress interaction, the pressure loss in the horizontal wellbore and perforation entry loss. The stress interaction and the wellbore pressure loss may induce different driving pressures for different fractures, which result in non-uniform fluid partitioning. Perforation entry loss effect can counterbalance the driving forces and promote uniform partitioning. The propagation regime determines the fluid flow and the interaction stress, which can also affect the propagation process. The influence of each effect is estimated as follows.

(a) The interaction stress σ_{int} between two fractures scales as $E'W/D$, where W is the characteristic fracture opening width assuming that the total pumping flux Q_0 is evenly partitioned into N fractures [20] and D is their distance.

For viscosity scaling, the characteristic fracture length L_m and opening width W_m are defined as [8]

$$L_m = \left(\frac{E' Q_p^3 t^4}{\mu'}\right)^{1/6}, \quad W_m = \left(\frac{\mu' Q_p^3 t^2}{E'}\right)^{1/6} \tag{70}$$

where $Q_p = Q_0/N$. The stress interaction effect varies with fractures length. So define $\kappa = L_m/D$ to characterize fracture length by the distance and $L_m = \kappa D$. The width W_m can be obtained as

$$W_m = \left(\frac{\mu' Q_p}{E'}\right)^{1/4} \cdot \sqrt{\kappa D} \tag{71}$$

and then the interaction stress σ_{int} for viscosity-dominated regime can be given as

$$\sigma_{int} \propto \sqrt{\kappa} \cdot \frac{E'^{3/4} Q_p^{1/4} \mu'^{1/4}}{\sqrt{D}} \tag{72}$$

For toughness scaling, the characteristic fracture length L_k and opening width W_k are defined as [8]

$$L_k = \left(\frac{E' Q_p t}{K'}\right)^{2/3}, \quad W_k = \left(\frac{K'^2 Q_p t}{E'^2}\right)^{1/3} \tag{73}$$

By similar derivation, σ_{int} for toughness-dominated regime can be given as

$$\sigma_{int} \propto \sqrt{\kappa} \cdot \frac{K'}{\sqrt{D}} \tag{74}$$

(b) The pressure loss in the wellbore can be estimated by substituting $V = Q_0/(\pi a^2)$ into Darcy–Weisbach equation Eq. (17), which can be written as

$$p_{wellbore} \propto f(Re, e) \cdot \frac{D\rho Q_0^2}{4\pi^2 a^5} \tag{75}$$

(c) The counterbalance pressure by the entry friction can be given as

$$p_{perf} \propto \varphi_p Q_p^2 \tag{76}$$

The fluid can be almost evenly partitioned if counterbalance pressure p_{perf} is in the same order with $\sigma_{int} + p_{wellbore}$, which can be written as

$$p_{perf} \propto \sigma_{int} + p_{wellbore} \tag{77}$$

In the early stage of propagation, $\kappa = L_m/D$ is relatively small and the interaction stress in Eqs. (72) or (74) is slight. The pressure loss in the wellbore is the main reason for pressure difference. As fractures propagate, σ_{int} increases and may become the dominating effect for pressure difference.

In order to quantitatively investigate the influences of propagation regimes, stress interaction, pressure loss in the wellbore and perforation entry loss in details, the simultaneous propagation of four HFs is modeled as shown in Fig. 11. We only consider the conditions that the maximum in situ stress is much larger than the minimum in situ stress, in which the fractures would propagate in the direction of the maximum in situ stress without kinking [20]. Even though the growth path is straight, the advantage of XFEM that the fracture fronts can locate inside the elements can still be revealed and this developed method can be easily extended to curve fractures. The parameters are given in Table 2. The initial lengths are 2.1 m and the four fractures are located with equal distance at $D_I = 10$ m, $I = 1, 2, 3$. The maximum and minimum in situ stresses are 10 and 0 MPa respectively. Any other minimum in situ stress can be superimposed on the current values and so only net pressure in the fractures is considered here. 20,205 quadrilateral elements are adopted to discretize the geometry.

Table 2 Parameters for simultaneous propagation of four HFs

E (GPa)	ν	σ_h (MPa)	σ_H (MPa)	Q_0 (m^3/s)	μ (Pa s)	ρ (kg/m^3)	a (m)	h (m)	D_I (m)
20	0.2	0	10	0.04	0.001	1000	0.05	20	10

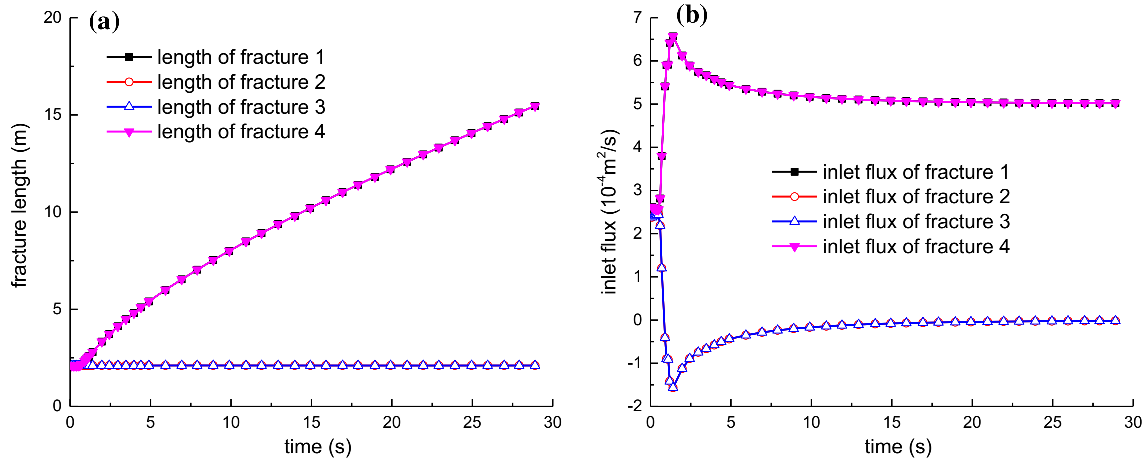

Fig. 12 Simulation results of the propagation of four HFs for $K_{Ic} = 3$ MPa $\sqrt{\text{m}}$ when the pressure loss in the wellbore and the perforation entry loss are negligible: the evolution of **a** fracture lengths and **b** inlet fluxes

6.2 Effect of stress interaction

Firstly, we focus on the influence of stress interaction on the propagation of multiple HFs. The pressure loss in the wellbore and the perforation entry loss are neglected, which means both p_{perf} and $p_{wellbore}$ are zero. The cases with $K_{Ic} = 3$ MPa $\sqrt{\text{m}}$ and $K_{Ic} = 1$ MPa $\sqrt{\text{m}}$ are simulated and the initial time increments are 0.1 and 0.3 s, respectively. The results are shown in Figs. 12 and 13. In both cases, fracture 1 and 4 propagate with the same velocity and so are fracture 2 and 3 because the pressure in the wellbore is uniform. The initial SIFs of the outer fractures, 1 and 4, are a little larger than those of the inner fractures, 2 and 3, because of the stress interaction among them. In both cases, the inner fractures would stop propagating finally because of the shielding effect from the outer fractures. Denoted by the open square symbols in Figs. 12b and 13b, the inlet fluxes into the inner fractures would evolve to zero, which means most of the fluid would flow into the outer fractures. The inlet fluxes of fracture 2 and 3 may even be negative, which means that the fluid in these fractures flows out of them and into the wellbore. As the outer fractures propagate and become longer, the inner fractures are shielded and squeezed. What's more, the driving pressure in the wellbore decreases gradually and the fluid in the inner fractures flows out. However, the fluid volumes in the inner fractures are finite and the outflow rates are quite small.

The inner fractures would stop propagating almost at the initial time for $K_{Ic} = 3$ MPa $\sqrt{\text{m}}$, which is toughness-dominated regime assuming the fluid is evenly partitioned. However, they would propagate to some distances before they stop for $K_{Ic} = 1$ MPa $\sqrt{\text{m}}$, which is close to viscosity-dominated regime. The phenomenon shows that the viscosity-dominated regime can promote simultaneous propagation of fractures compared with toughness-dominated regime. In viscosity-dominated regime, the fluid flow in the fractures dominates the fractures growth and the effect of interaction stress is relatively small.

6.3 Effect of pressure loss in the wellbore

The pressure loss in the horizontal wellbore is included. The simulation results are shown in Figs. 14 and 15 for $K_{Ic} = 3$ MPa $\sqrt{\text{m}}$ and $K_{Ic} = 1$ MPa $\sqrt{\text{m}}$, respectively. Different from the results neglecting the pressure loss in the wellbore, all the four fractures propagate with different velocities. Fracture 4 propagates more slowly than fracture 1 because of the pressure loss in the wellbore and most of the fluid would finally flow into fracture 1. The evolution of SIFs for four fractures with $K_{Ic} = 3$ MPa $\cdot \sqrt{\text{m}}$ is shown in Fig. 14c. Fracture 1 is always propagating and K_I for fracture 1 is always equal to K_{Ic}. Fracture 4 propagates for a short period of time and after that K_I for fracture 4 drops below K_{Ic}. The number of secant iteration is shown in Fig. 14d. The evolutions of fracture lengths and K_I demonstrate the capability of the secant iteration method for determining the fracture lengths based on SIFs.

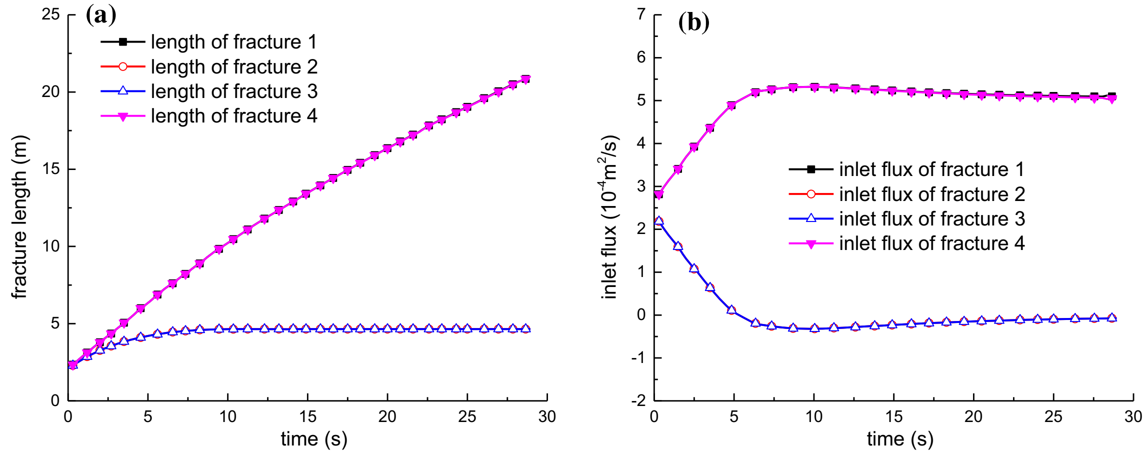

Fig. 13 Simulation results of the propagation of four HFs for $K_{Ic} = 1$ MPa $\sqrt{\text{m}}$ when the pressure loss in the wellbore and the perforation entry loss are negligible: the evolution of **a** fracture lengths and **b** inlet fluxes

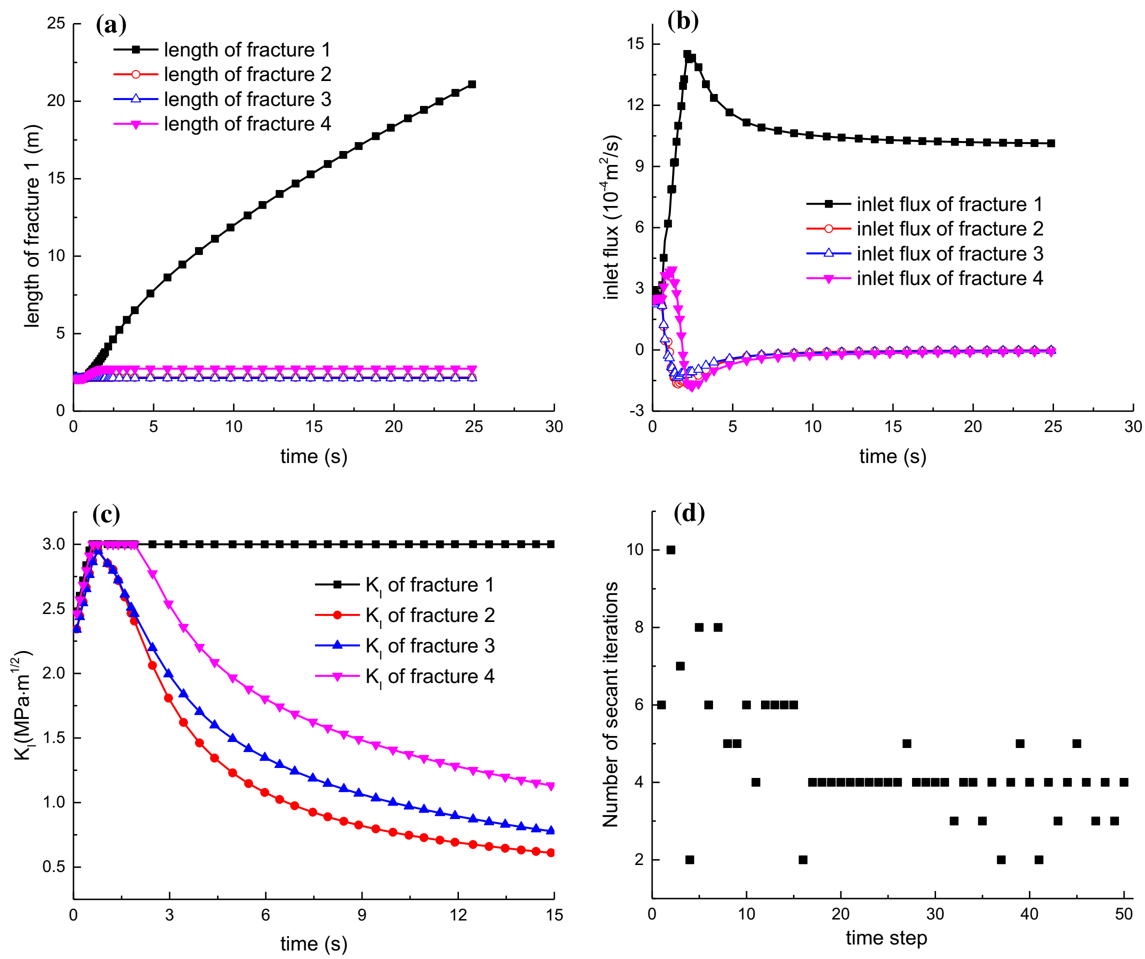

Fig. 14 Simulation results of the propagation of four HFs for $K_{Ic} = 3$ MPa $\sqrt{\text{m}}$ when the perforation entry loss is negligible: the evolution of **a** fracture lengths, **b** inlet fluxes and **c** K_I; **d** the number of secant iterations for fracture lengths

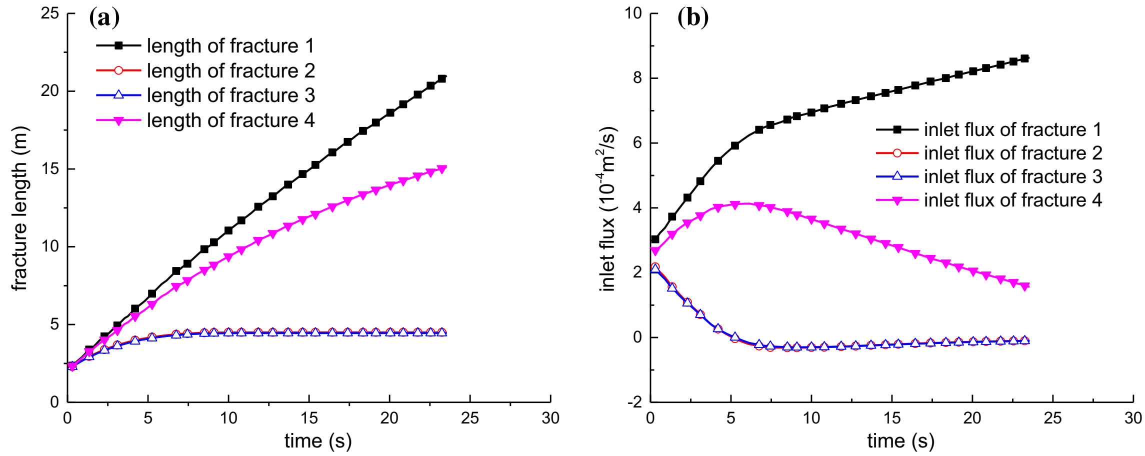

Fig. 15 Simulation results of the propagation of four HFs for $K_{Ic} = 1$ MPa $\sqrt{\text{m}}$ when the perforation entry loss is negligible: the evolution of **a** fracture lengths and **b** inlet fluxes

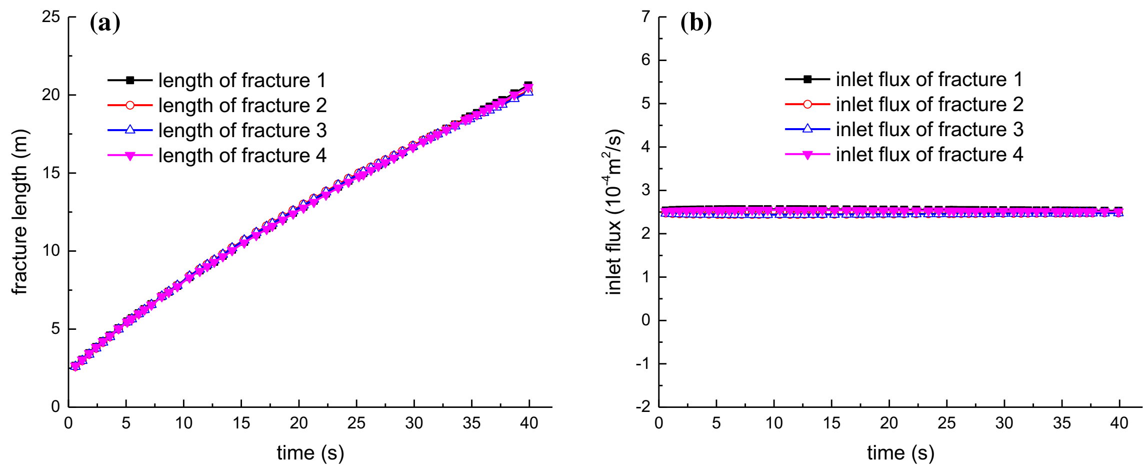

Fig. 16 Simulation results of the propagation of four HFs for $K_{Ic} = 1$ MPa $\sqrt{\text{m}}$ and $\phi_p = 10^4$ MPa s^2/m^6: the evolution of **a** fracture lengths and **b** inlet fluxes

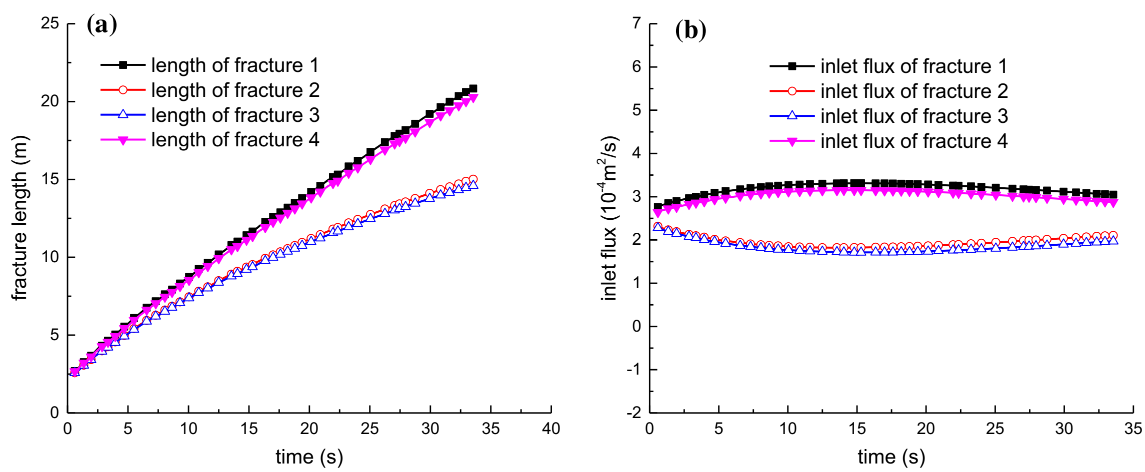

Fig. 17 Simulation results of the propagation of four HFs for $K_{Ic} = 1$ MPa $\sqrt{\text{m}}$ and $\phi_p = 10^3$ MPa s^2/m^6: the evolution of **a** fracture lengths and **b** inlet fluxes

6.4 Effect of perforation entry loss

As shown in Eq. (77), if the pressure loss at the perforations can counteract the interaction stress and wellbore pressure loss, the fluid is tend to be evenly partitioned. As an examination, we substitute the parameters in this simulation into Eq. (77) for $K_{Ic} = 1\,\mathrm{MPa}\sqrt{\mathrm{m}}$ and $\kappa = 1$. We can obtain $\sigma_{int} \propto 1\,\mathrm{MPa}$, $p_{wellbore} \propto 0.01\,\mathrm{MPa}$, $p_{perf} \propto \varphi_p \cdot 10^{-4}\,\mathrm{m}^6\,\mathrm{s}^{-2}$. Because we have adopted a model for relatively smooth pipes, the pressure loss in the wellbore is relatively small. By the estimation, perforations with $\varphi_p \propto 10^4\,\mathrm{MPa\,s^2/m^6}$ can lead to nearly uniform partitioning. The numerical results with $\varphi_p = 10^4\,\mathrm{MPa\,s^2/m^6}$ and $\varphi_p = 10^3\,\mathrm{MPa\,s^2/m^6}$ are shown in Figs. 16 and 17. With $\varphi_p = 10^4\,\mathrm{MPa\,s^2/m^6}$, the fluid is evenly partitioned and all the fractures propagate with almost the same lengths. When φ_p is $10^3\,\mathrm{MPa\,s^2/m^6}$, even though the fluid can't be evenly partitioned, it has been greatly improved compared with the cases in Fig. 15 without entry loss. The effect of the pressure loss in the wellbore is nearly eliminated. For $K_{Ic} = 3\,\mathrm{MPa}\sqrt{\mathrm{m}}$, similar results can be obtained.

7 Conclusions

In this paper, a fully coupled model is established for the simultaneous propagation of multiple HFs. The deformation of the solid medium, the propagation of fractures, the fluid flow in fractures, the flow in the wellbore and the pressure loss at the perforations are all considered. XFEM is adopted to model arbitrary propagation of fractures, which can allow the location of fracture front inside the element and easily deal with anisotropy or heterogeneous materials. In order to solve the fully coupled nonlinear equations efficiently, Newton's iteration is proposed to solve the equations. A secant iteration is adopted to determine the new positions of fracture fronts. The viscosity-dominated and toughness-dominated regimes are simulated and compared with the semi-analytical solutions. The analytical solution of two inviscid-fluid-driven fractures initiation is derived and also modeled with the newly developed method. The good agreements of numerical results and analytical solutions demonstrate the accuracy of the method.

For the propagation of multiple HFs in each fracturing stage, uniform fluid partitioning and fracture propagation with the same lengths are desired in engineering application. The propagation regime, stress interaction between different fractures, pressure loss in the wellbore and the perforation entry loss interplay together to influence the whole propagation process. Generally, the stress interaction and the pressure loss in the wellbore are two sources disturbing uniform driving forces and may induce preferential growth. The perforation entry loss can compete with the stress interaction and the wellbore pressure loss and counterbalance the pressures to guarantee uniform partitioning. An magnitude estimation and numerical simulations are conducted to investigate the effect of these factors.

In practice, other effects which can disturb fracture driving forces include different fracture lengths, different tectonic stresses, heterogeneity of the formations and so on. The entry loss coefficients may also vary among perforation clusters. All these effects may induce different propagation velocities for multiple HFs and it's cumbersome to obtain uniform partitioning. Even though a large entry loss coefficient can promote uniform partitioning, it would increase the pumping operation pressure which is limited by the operation equipment and so a proper entry loss coefficient should be designed carefully.

Acknowledgements This work is supported by National Natural Science Foundation of China (Grant Nos. 11532008 and 11372157), the Special Research Grant for Doctor Discipline by Ministry of Education, China (Grant No. 20120002110075), the Foundation for the Author of National Excellent Doctoral Dissertation of China (Grant No. 201326). Tsinghua University Initiative Scientific Research Program is also acknowledged.

Appendix: Fluid partitioning into two HFs

Assume two stationary fractures in linear-elastic solid medium are interconnected by a wellbore with zero friction. The geometry is symmetric with respect to the wellbore. The half lengths are denoted as l_1 and l_2. Pump inviscid fluid into the two fractures from the wellbore with the given flux Q_0. The pressure in the wellbore is uniform with the value p_w and the pressure in each fracture is also uniform with the values of p_1 and p_2, respectively. The inlet fluxes into the two fractures are denoted as $2q_1$ and $2q_2$. Plane strain assumption is adopted and the heights of the fractures are h. The mass conservation can be given by

$$2hq_1 + 2hq_2 = Q_0 \tag{78}$$

At the inlets, the entry loss characterized by a coefficient φ_p is considered and then

$$p_w - p_1 = \varphi_p \cdot (2hq_1)^2 \tag{79}$$

$$p_w - p_2 = \varphi_p \cdot (2hq_2)^2 \tag{80}$$

Assume there's no stress interaction effect between the fractures and then from the theoretical solution of a fracture loaded by uniform pressure, the whole volume of the fluid in the fracture is

$$V = \frac{2(\kappa+1)\pi h l^2}{8\mu} p \tag{81}$$

where $\kappa = 3 - 4\nu$ and $\mu = E/[2(1+\nu)]$. Consider the process before the propagation of the fractures and the inlet flow rate for each fracture can be given as

$$q_i = \frac{\dot{V}_i}{2h} = c_i \dot{p}_i, \quad i = 1, 2 \tag{82}$$

where $c_i = (\kappa + 1)\,\pi l_i^2/\,(8\mu)$.

The initial conditions are given as

$$p_1(0) = p_2(0) = p_0 \tag{83}$$

Combining Eqs. (78), (79), (80), (82) and (83), we can solve the equations and get the fluxes as

$$q_1 = \left[-\frac{c_1 - c_2}{2\,(c_1 + c_2)} e^{-\eta t} + \frac{c_1}{c_1 + c_2}\right] \cdot \frac{Q_0}{2h} \tag{84}$$

$$q_2 = \left[\frac{c_1 - c_2}{2\,(c_1 + c_2)} e^{-\eta t} + \frac{c_2}{c_1 + c_2}\right] \cdot \frac{Q_0}{2h} \tag{85}$$

where $\eta = (c_1 + c_2)\,/\,\left(4c_1c_2\varphi_p h Q_0\right)$. When $t = 0$, $q_1 = q_2 = Q_0/\,(4h)$ and when $t \to \infty$, $q_1 = c_1/\,(c_1 + c_2) \cdot Q_0/\,(2h)$, $q_2 = c_2/\,(c_1 + c_2) \cdot Q_0/\,(2h)$. So we can define the critical time $t_c = 1/\eta = 4c_1c_2\varphi_p h Q_0/\,(c_1 + c_2)$ to characterize the evolution of fluid partitioning.

References

1. Zhang X, Bunger AP, Jeffrey RG (2014) Mechanics of two interacting magma-driven fractures: a numerical study. J Geophys Res Solid Earth 119:8047–8063. doi:10.1002/2014jb011273
2. Lucantonio A, Noselli G, Trepat X, DeSimone A, Arroyo M (2015) Hydraulic fracture and toughening of a brittle layer bonded to a hydrogel. Phys Rev Lett 115:188105. doi:10.1103/PhysRevLett.115.188105
3. Khristianovic SA, Zheltov YP (1955) Formation of vertical fractures by means of highly viscous liquid. Paper presented at the proceedings of 4th world petroleum congress, Rome, Italy
4. Geertsma J, De Klerk F (1969) A rapid method of predicting width and extent of hydraulically induced fractures. J Pet Technol 21:1571–1581. doi:10.2118/2458-PA
5. Perkins TK, Kern LR (1961) Widths of hydraulic fractures. J Pet Technol 13:937–949. doi:10.2118/89-PA
6. Nordgren RP (1972) Propagation of a vertical hydraulic fracture. Soc Pet Eng J 12:306–314. doi:10.2118/3009-PA
7. Spence DA, Sharp P (1985) Self-similar solutions for elastohydrodynamic cavity flow. In: Proceedings of the royal society of london series A, mathematical and physical sciences, vol 400, pp 289–313
8. Adachi J (2001) Fluid-driven fracture in permeable rock. Dissertation, University of Minnesota
9. Savitski AA, Detournay E (2002) Propagation of a penny-shaped fluid-driven fracture in an impermeable rock: asymptotic solutions. Int J Solids Struct 39:6311–6337. doi:10.1016/S0020-7683(02)00492-4
10. Detournay E (2004) Propagation regimes of fluid-driven fractures in impermeable rocks. Int J Geomech 4:35–45. doi:10.1061/(ASCE)1532-3641(2004)4:1(35)
11. Garagash DI (2006) Propagation of a plane-strain hydraulic fracture with a fluid lag: early-time solution. Int J Solids Struct 43:5811–5835. doi:10.1016/j.ijsolstr.2005.10.009
12. Bažant ZP, Ohtsubo H, Aoh K (1979) Stability and post-critical growth of a system of cooling or shrinkage cracks. Int J Fracture 15:443–456. doi:10.1007/bf00023331
13. Nemat-Nasser S, Keer LM, Parihar KS (1978) Unstable growth of thermally induced interacting cracks in brittle solids. Int J Solids Struct 14:409–430. doi:10.1016/0020-7683(78)90007-0
14. Nemat-Nasser S, Sumi Y, Keer LM (1980) Unstable growth of tension cracks in brittle solids: stable and unstable bifurcations, snap-through, and imperfection sensitivity. Int J Solids Struct 16:1017–1035. doi:10.1016/0020-7683(80)90102-x
15. Bažant ZP, Tabbara MR (1992) Bifurcation and stability of structures with interacting propagating cracks. Int J Fracture 53:273–289. doi:10.1007/bf00017341
16. Olson JE, Taleghani AD (2009) Modeling simultaneous growth of multiple hydraulic fractures and their interaction with natural fractures. Paper presented at the SPE hydraulic fracturing technology conference society of petroleum engineers, The Woodlands, Texas
17. Taleghani AD (2011) Modeling simultaneous growth of multi-branch hydraulic fractures. Paper presented at the 45th US rock mechanics/geomechanics symposium American rock mechanics association, San Francisco, California
18. Mack MG, Elbel JL, Piggott AR (1992) Numerical representation of multilayer hydraulic fracturing. Paper presented at the 33th US symposium on rock mechanics (USRMS) American rock mechanics association, Santa Fe, New Mexico
19. Bunger AP (2013) Analysis of the power input needed to propagate multiple hydraulic fractures. Int J Solids Struct 50:1538–1549. doi:10.1016/j.ijsolstr.2013.01.004
20. Lecampion B, Desroches J (2015) Simultaneous initiation and growth of multiple radial hydraulic fractures from a horizontal wellbore. J Mech Phys Solids 82:235–258. doi:10.1016/j.jmps.2015.05.010
21. Wu K, Olson JE (2015) Mechanisms of simultaneous hydraulic-fracture propagation from multiple perforation clusters in horizontal wells. SPE J 21:1–9. doi:10.2118/178925-PA
22. Gordeliy E, Peirce A (2013) Coupling schemes for modeling hydraulic fracture propagation using the XFEM. Comput Methods Appl Mech Eng 253:305–322. doi:10.1016/j.cma.2012.08.017
23. Gordeliy E, Peirce A (2013) Implicit level set schemes for modeling hydraulic fractures using the XFEM. Comput Methods Appl Mech Eng 266:125–143. doi:10.1016/j.cma.2013.07.016
24. Khoei AR, Hirmand M, Vahab M, Bazargan M (2015) An enriched FEM technique for modeling hydraulically driven cohesive fracture propagation in impermeable media with frictional natural faults: numerical and experimental investigations. Int J Numer Methods Eng 104:439–468. doi:10.1002/nme.4944
25. Gupta P, Duarte CA (2016) Coupled formulation and algorithms for the simulation of non-planar three-dimensional hydraulic fractures using the generalized finite element method. Int J Numer Anal Methods Geomech 40:1402–1437. doi:10.1002/nag.2485
26. Faivre M, Paul B, Golfier F, Giot R, Massin P, Colombo D (2016) 2D coupled HM-XFEM modeling with cohesive zone model and applications to fluid-driven fracture network. Eng Fract Mech 159:115–143. doi:10.1016/j.engfracmech.2016.03.029
27. Mohammadnejad T, Khoei AR (2013) An extended finite element method for fluid flow in partially saturated porous media with weak discontinuities; the convergence analysis of local enrichment strategies. Comput Mech 51:327–345. doi:10.1007/s00466-012-0732-8
28. Wu K (2014) Numerical modeling of complex hydraulic fracture development in unconventional reservoirs. Dissertation, The University of Texas at Austin
29. Gordeliy E, Detournay E (2011) A fixed grid algorithm for simulating the propagation of a shallow hydraulic fracture with a fluid lag.

Int J Numer Anal Methods Geomech 35:602–629. doi:10.1002/nag.913
30. Adachi J, Siebrits E, Peirce A, Desroches J (2007) Computer simulation of hydraulic fractures. Int J Rock Mech Min Sci 44:739–757. doi:10.1016/j.ijrmms.2006.11.006
31. Peirce A, Detournay E (2008) An implicit level set method for modeling hydraulically driven fractures. Comput Methods Appl Mech Eng 197:2858–2885. doi:10.1016/j.cma.2008.01.013
32. Xu DD, Liu ZL, Liu XM, Zeng QL, Zhuang Z (2014) Modeling of dynamic crack branching by enhanced extended finite element method. Comput Mech 54:489–502. doi:10.1007/s00466-014-1001-9
33. Fox RW, McDonald AT, Pritchard PJ (2010) Introduction to fluid mechanics. Wiley, New York
34. Moody LF (1944) Friction factors for pipe flow. Trans ASME 66:671–684
35. Colebrook CF (1939) Turbulent flow in pipes, with particular reference to the transition region between the smooth and rough pipe laws. J Inst Civ Eng 11:133–156. doi:10.1680/ijoti.1939.13150
36. Swamee PK, Jain AK (1976) Explicit equations for pipe-flow problems. J Hydraul Div Asce 102:657–664
37. Haaland SE (1983) Simple and explicit formulas for the friction factor in turbulent pipe flow. J Fluids Eng 105:89–90. doi:10.1115/1.3240948
38. Crump JB, Conway MW (1988) Effects of perforation-entry friction on bottomhole treating analysis. J Pet Technol 40:1041–1048. doi:10.2118/15474-PA
39. Cramer DD (1987) The application of limited-entry techniques in massive hydraulic fracturing treatments. Paper presented at the SPE production operations symposium, Oklahoma City, Oklahoma
40. McDaniel BW, Willett RM, Underwood PJ (1999) Limited-entry frac applications on long intervals of highly deviated or horizontal wells. Paper presented at the SPE annual technical conference and exhibition, Houston, Texa
41. Moës N, Dolbow J, Belytschko T (1999) A finite element method for crack growth without remeshing. Int J Numer Methods Eng 46:131–150. doi:10.1002/(sici)1097-0207(19990910)46:1<131::aid-nme726>3.3.co;2-a
42. Fries T-P, Belytschko T (2010) The extended/generalized finite element method: an overview of the method and its applications. Int J Numer Methods Eng 84:253–304. doi:10.1002/nme.2914
43. Zeng QL, Liu ZL, Xu DD, Wang H, Zhuang Z (2016) Modeling arbitrary crack propagation in coupled shell/solid structures with X-FEM. Int J Numer Methods Eng 106:1018–1040. doi:10.1002/nme.5157
44. Gordeliy E, Peirce A (2015) Enrichment strategies and convergence properties of the XFEM for hydraulic fracture problems. Comput Methods Appl Mech Eng 283:474–502. doi:10.1016/j.cma.2014.09.004
45. Zhuang Z, Liu Z, Cheng B, Liao J (2014) Extended finite element method. Elsevier, Tsinghua University Press, Oxford
46. Dolbow J, Moës N, Belytschko T (2001) An extended finite element method for modeling crack growth with frictional contact. Comput Methods Appl Mech Eng 190:6825–6846. doi:10.1016/S0045-7825(01)00260-2
47. Gosz M, Moran B (2002) An interaction energy integral method for computation of mixed-mode stress intensity factors along non-planar crack fronts in three dimensions. Eng Fract Mech 69:299–319. doi:10.1016/s0013-7944(01)00080-7
48. Walters MC, Paulino GH, Dodds RH (2005) Interaction integral procedures for 3-D curved cracks including surface tractions. Eng Fract Mech 72:1635–1663. doi:10.1016/j.engfracmech.2005.01.002